# ELECTRON SPIN RESONANCE OF RUBY, ATOMIC HYDROGEN, AND CARBON NANOTUBES

Candidate Number: 630433
Project Number: CMP17
Supervisor: Prof RJ Nicholas
Word Count: 6925

# Electron spin resonance of ruby, atomic hydrogen, and carbon nanotubes

CMP17      Candidate Number: 630433      Supervisor: Prof RJ Nicholas

**Abstract**

Calibration and optimization of the recently re-engineered ESR spectrometer is achieved by taking measurements on four samples: ruby, hydrogen in $CaF_2$, hydrogen in $SrF_2$, and deuterium in $CaF_2$. Parameters of each system's Hamiltonian are determined from the ESR spectra, and the results obtained agree well with previous studies and, in the case of ruby, my own computer model. For the deuterium sample, spectra are modelled by manipulating experimentally obtained hydrogen spectra, and from this the electron-deuteron hyperfine coupling is determined as $233.2 \pm 2.5$ MHz for a spectrum obtained at high pressure. The calibration facilitates an ESR study of a solution of polymer-wrapped single-walled carbon nanotubes (SWNT-P3HT) coated on a quartz film. A broad, prominent transition line of width $\Delta_{FWHM} \sim 0.13$T is observed, and the position of this transition is found to have angular dependence. Extremal g-factor values of $g_\parallel = 2.058 \pm 0.003$ and $g_\perp = 2.073 \pm 0.003$ are obtained. The presence of this resonance is believed to be due to itinerant electrons on the walls of the nanotubes.
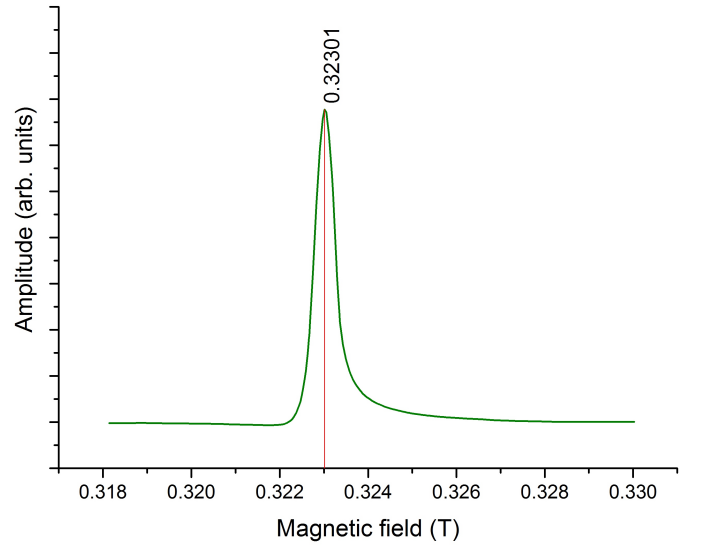
## 1   Introduction

Electron spin resonance (ESR) spectroscopy is an experimental technique used to analyse the energy level structure of electrons and ions in materials. In an ESR experiment, the specimen to be studied is placed in a static and uniform magnetic field **B**, and is illuminated with microwave radiation. The magnetic field splits the energy levels via the *Zeeman effect*. The aim is to then bring the microwave frequency into resonance with the energy level separation, in which case the specimen will absorb microwave energy. The intensity of the radiation after it has passed through the specimen is monitored and resonances are identified by observing the absorption extrema in this signal.

To better understand how an ESR experiment works, it is best to consider a simple example. Figure 1 shows the resulting spectrum of an ESR experiment I carried out on a DPPH (2,2-diphenyl-1-picrylhydrazyl) specimen. DPPH is a free radical, i.e. it has unpaired electrons which behave like free spins when placed in a magnetic field. In a semiclassical interpretation, the field causes the magnetic moment of each unpaired electron to precess around the field direction at the Larmor frequency $\nu_L = \frac{g\mu_B B}{h}$, where $g$ is the electron's g-factor (characteristic of its magnetic moment), $B = |\mathbf{B}|$, and $\mu_B = \frac{e\hbar}{2m_e}$ is the Bohr magneton. When the frequency of the incident microwaves matches the Larmor frequency, electrons can absorb radiation and, consequently, an absorption extremum is observed. Note that here, and throughout this project, the microwave frequency is held constant and resonance is found by sweeping the magnetic field. The resonance condition is

$$h\nu = h\nu_L = g\mu_B B, \qquad (1)$$

where $\nu$ is the microwave frequency.

This can also be thought of quantum mechanically.



**Figure 1:** ESR spectrum of DPPH. A single intense, narrow resonance is observed where the Zeeman splitting of the unpaired electrons in the sample matches the energy of the incident microwave radiation. This spectrum is used to aid calibration of the magnetic field, as described in Appendix A.

The Hamiltonian describing the energy levels is

$$H = -\boldsymbol{\mu}\cdot\mathbf{B} = g\mu_B\mathbf{B}\cdot\mathbf{J}, \qquad (2)$$

where $\boldsymbol{\mu} = -g\mu_B\mathbf{J}$ is the electron's magnetic moment, and $\mathbf{J}$ its angular momentum. $\mathbf{J}$ is quantized along the direction of $\mathbf{B}$ so that the energy levels can be written as

$$E(M_J) = g\mu_B B M_J, \qquad (3)$$

where $M_J = -J, -J+1, \ldots, J-1, J$. The microwaves induce magnetic dipole transitions between the levels subject to the selection rule $\Delta M_J = \pm 1$. Thus the resonance condition is

$$h\nu = |E(M_J) - E(M_J \pm 1)| = g\mu_B B \qquad (4)$$

in agreement with Equation (1).

Most materials do not have as simple an ESR spectrum as DPPH. Various atomic and electronic interactions can lead to rich energy level structures, which produce more intricate spectra. The effects of hyperfine and crystal field interactions are of particular importance in this report.

The primary aim of this project is to optimise the performance of the recently re-engineered ESR spectrometer for use on the 3rd year physics undergraduate practical course. To this end, I use the spectrometer to take a measurement series on four samples:

1. **Ruby**
   An $Al_2O_3$ crystal doped with $Cr^{3+}$ ions.

2. **CaF$_2$:H**
   A $CaF_2$ crystal containing hydrogen atoms on interstitial lattice sites.

3. **SrF$_2$:H**
   A $SrF_2$ crystal containing hydrogen atoms on interstitial lattice sites.

4. **CaF$_2$:D**
   A $CaF_2$ crystal containing deuterium atoms on interstitial lattice sites.

The majority of this report focuses on each of these samples in turn, in the above order. In each case, a theoretical framework is provided through the construction of a *spin Hamiltonian*, i.e. a Hamiltonian built of quantum-mechanical spin operators. By diagonalizing the Hamiltonian, predictions are made about the appearance of the ESR spectra. Experimental data is then presented and compared to those predictions, and relevant parameters are calculated.

ESR studies of ruby have previously been carried out by Schulz-Dubois[1] and Collins et al[2]. I determine values for the g-factor and the crystal field splitting $D$ from my data, and agreement is found with these previous studies, to within the margin of uncertainty. Interpretation in previous studies relies on independent determination of the orientation of the ruby sample's crystallographic axis (c-axis). To eradicate this necessity, I build a computer model capable of computing the position of all resonances for any orientation of the crystal. My experimental data is fitted to this model successfully.

For CaF$_2$:H and SrF$_2$:H, calculated parameters agree well with previous ESR studies carried out by Hall and Schumacher[3] (H&S), Hodby[27] and Welber[4]. H&S also give results for a CaF$_2$:D sample. To advance their work, I construct model CaF$_2$:D spectra by manipulating experimentally obtained CaF$_2$:H spectra. I do not believe this technique has been used before, and I use it to obtain a value of $233.2\pm2.5$ MHz

for the electron-proton hyperfine coupling from a spectrum obtained at 4106 bar, suggesting a correction to the value obtained by H&S.

Through study of these samples, the various settings on the ESR kit are optimised to produce well-resolved spectra with low signal-to-noise ratios, and the magnetic field is well calibrated. This facilitates the study of a single-walled carbon nanotube (SWNT) specimen. A discussion of the experiments carried out on this specimen follows that of the CaF$_2$:D sample, and completes the main body of the report.
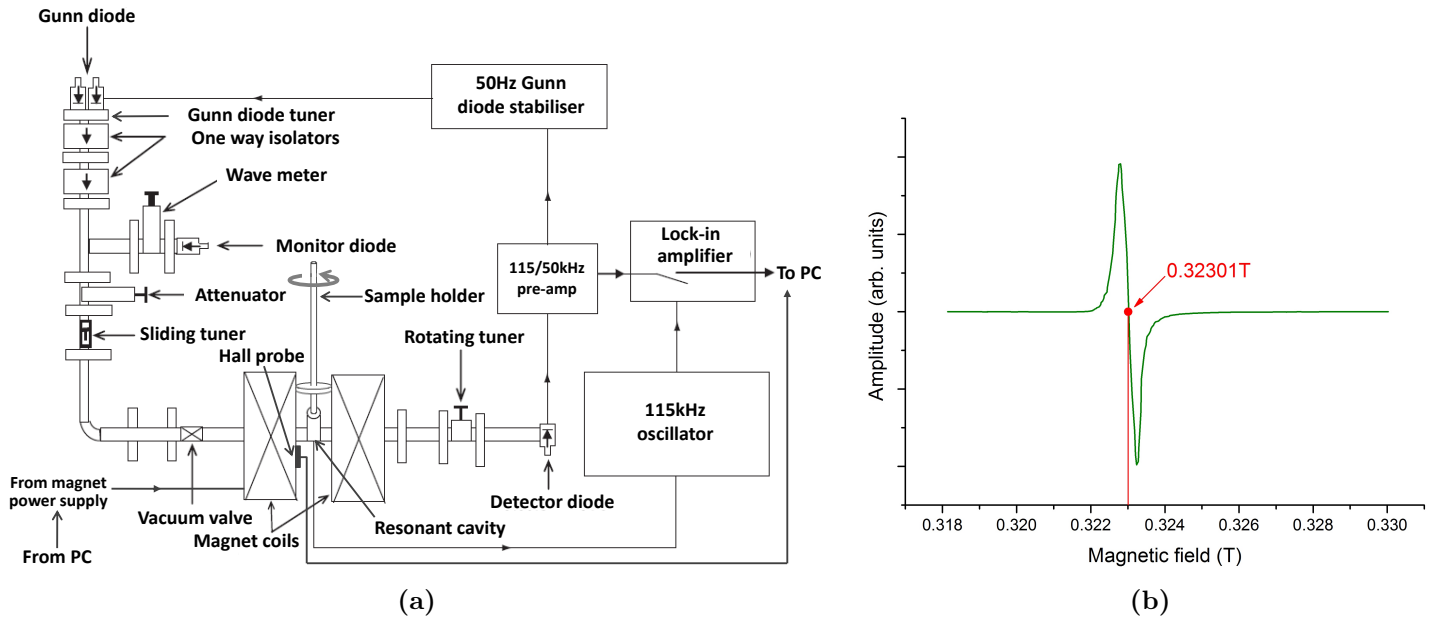
Since the discovery of SWNTs[5–7], there has been significant research into their extraordinary electrical and optical properties[8,9]. The particular sample studied here is a nanohybrid structure of semiconducting SWNTs wrapped in the semiconducting polymer poly(3-hexylthiophene) (P3HT), described by Schuettfort[10]. The polymer serves to prevent bundling of different types of SWNTs so that only nanotubes with a small range of diameter ($\sim$1nm) and chiral angle are present, and individual nanotubes are isolated from one another[10–12]. The SWNT-P3HT composite has potential application in organic photovoltaic (OPV) devices[13], which are markedly cheaper to produce compared to conventional silicon-based products. To date, the most efficient OPV solar cell produced has a power conversion efficiency (PCE) of 10.6%[14] (c.f. 24.7% for silicon cells[15]).

The remarkable carrier mobility of SWNTs[16] makes them a prime candidate for incorporation into such solar cells[17], though only small efficiencies have been achieved to date. Lanzi et al[18] report a PCE of 0.52% for a cell with a SWNT-P3HT blend used in the active layer. Clearly further research and development is required, motivating an ESR investigation from which we may learn about the electronic properties of the SWNT-P3HT composite. A broad, asymmetric lineshape is found at $g \approx 2.06$, and a slight g-factor anisotropy is observed. It is posited that the source of this line is itinerant electrons on the nanotube walls. Corzilius[19] and Chipara[20] have found similarly positioned lines in ESR studies of a fullerene-SWNT composite and polyethylene-SWNT composite respectively.

Before proceeding to discussion of the five samples, I describe the experimental apparatus used.

## 2 Experimental Apparatus and Techniques

The apparatus is shown in Figure 2a. X-band microwave radiation from a *Gunn diode* propagates toward a *resonant cavity* via a rectangular waveguide. An *absorption wave meter* is used to determine the microwave frequency $\nu$ – I measure $\nu = (9.25\pm0.01)$ GHz,

**Figure 2:** (a) Diagram of apparatus used to measure ESR spectra (taken from the lab script SS12 [21], with some additions). (b) Derivative with respect to field of the ESR transition in DPPH, as observed when phase-sensitive detection is employed.

and this frequency is used exclusively in my investigations. An *attenuator* can be used to limit the wave power transmitted to the cavity.

The magnetic field is provided by two large coils driven by a *magnet power supply*, which provides currents up to a maximum of 20 A. The supply is routed to a PC on which software is used to steadily sweep the current up and down. A Hall probe was introduced to the apparatus at the start of the 2014/15 academic year to provide measurement of magnetic field strength. It is affixed to the inside wall of one of the coils. The signal from the Hall probe is fed to the PC so that spectra can be instantly plotted as functions of magnetic field. The magnetic field strength must be calibrated. The main source of uncertainty in the field calibration stems from the relationship between field and Hall voltage deviating slightly from linearity. The deviation is small however – $\mathcal{O}(10^{-5}\,\mathrm{T})$ – and the ease with which this method allows data to be recorded far outweighs the slight inaccuracy incurred. Further details of the calibration are provided in Appendix A.

The specimen under investigation is placed in the end of a long, plastic sample holder and inserted into the cavity from above. In this way, the sample can be rotated about the vertical axis. To obtain the clearest signals, the cavity must be tuned so as to resonate with the microwave radiation. This is done by varying the effective size of the cavity using three components: the *rotating tuner*, the *sliding tuner* and the *Gunn diode tuner*.

The absorption amplitude is measured by the *detector diode*. At resonance, the sample absorbs radiation so that less reaches the diode, and thus an absorption

extremum is recorded.

Phase-sensitive detection is employed to improve the signal-to-noise ratio of the signal. A consequence of this is that the recorded signal actually looks like the *derivative* of the absorption spectrum with respect to field (Figure 2b). This is discussed in Appendix B.
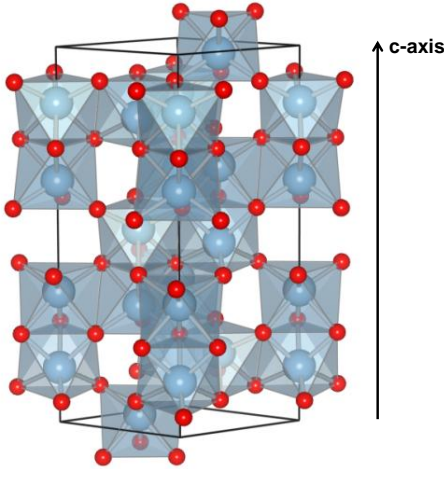
A software package has been built on the PC to control data acquisition and enable ESR spectra to be easily plotted. The software allows the range of magnet current that is to be swept to be specified, along with the total sweep time $T$. The lock-in amplifier has a variable time constant, $\tau$, which determines how frequently data points are recorded in the time domain. The choice of time period and time constant together determines how frequently data points are recorded in the field domain, as the field is swept. For transitions that are narrow or closely spaced, it is important that data points are recorded often enough for the transitions to be well resolved. As such, long sweep times are needed to properly observe intricate spectra. Different combinations of sweep times and time constants were experimented with in order to obtain the best possible signals. I state the settings used to obtain each spectrum in the succeeding sections of this report.

The collected data were analysed using the *Origin-Pro* data analysis package.

# 3 Ruby

## 3.1 Theory and background

Study of the ruby sample is undertaken by 3rd year students doing the "mini-project" extension of the un-

**Figure 3:** Crystal structure of corundum, with the crystallographic axis labelled. Red spheres are $O^{2-}$ ions, blue spheres are $Al^{3+}$ ions. In ruby, a small amount of the $Al^{3+}$ ions are substituted with $Cr^{3+}$ ions. Image taken from the *Crystallography365* online blog[22].

dergraduate practical SS12[21], and I discuss my own investigation here. A theoretical background is first provided, following Collins et al. It is hoped that the following could be modified for use as a primer for students carrying out this practical in the future.

The crystal structure of ruby is that of corundum (crystalline $Al_2O_3$), but with a small number of the $Al^{3+}$ ions substituted by $Cr^{3+}$ ions (see Figure 3). Energy levels of the $Cr^{3+}$ ions are studied in the ESR experiment. Each $Cr^{3+}$ ion is subjected to a strong electric field created by its six neighbouring $O^{2-}$ ions, and this significantly affects the energy levels of the $Cr^{3+}$ ions.

Pryce developed a formalism for deriving the spin Hamiltonian of a paramagnetic ion in a crystal field using a modified perturbation theory[23]. For the ruby crystal, this leads to a so-called *effective spin* Hamiltonian

$$H = g\mu_B \mathbf{B} \cdot \mathbf{S} + D\left(\frac{5}{4} - S_z^2\right), \quad (5)$$

where $D$ is the *zero-field splitting*. The crystal field splits the free-ion ground state into two degenerate states corresponding to $M_S = \pm 3/2$ and $M_S = \pm 1/2$, separated by $2D$. Application of the magnetic field removes the remaining spin degeneracy, giving four levels labelled by $M_S$. A more thorough explanation is provided in Appendix C. We expect to observe transitions between these four levels in our experiment.

The crystal symmetry makes the g-factor anisotropic. The symmetry is uniaxial, so the g-factor tensor can be specified by two components: $g_\parallel$ for $\mathbf{B}$ parallel to $z$, and $g_\perp$ for $\mathbf{B}$ perpendicular to $z$. Thus the Hamiltonian is written

$$H = g_\perp \mu_B (B_x S_x + B_y S_y)$$
$$+ g_\parallel \mu_B B_z S_z + D(\frac{5}{4} - S_z^2). \quad (6)$$

Because of the symmetry, $\mathbf{B}$ can be chosen to lie in the $x$-$z$ plane without loss of generality. With $\theta$ the angle between $\mathbf{B}$ and $z$ we have

$$H = g_\perp \mu_B B S_x \sin\theta + g_\parallel \mu_B B S_z \cos\theta + D(\frac{5}{4} - S_z^2). \quad (7)$$

It should be noted that $D$ and the components of $g$ have been shown[25] to have a slight dependence on $\mathbf{B}$ and $\nu$; a first approximation of them being constant will suffice here.

The Hamiltonian can be diagonalized using a linear combination of the spin eigenstates, $|\phi_n\rangle = \sum_j A_{ij} |j\rangle$. This leads to a quartic equation for the eigenvalues, which is derived in Appendix C. I wrote a program to solve this equation numerically using Newton-Raphson iteration, enabling energy level diagrams to be plotted as a function of $B$ for any angle $\theta$ (see Appendix E). The nature of the levels changes as a function of $\theta$ – this suggests that the position and intensity of the ESR transitions should change as the sample is rotated.

I extended this program to compute the energy levels for a range of $B$ and $\theta$ and, at each computation, calculate the energy differences between the four levels. Whenever this matches (to within $0.02\,\mathrm{GHz}$) the frequency of the incident microwave radiation, the corresponding values of $B$ and $\theta$ are written to an output file. With this, a theoretical *resonance field* is produced, where the field positions of the resonances are plotted as a function of $\theta$. Such a plot is compared to experimental data in the following section.
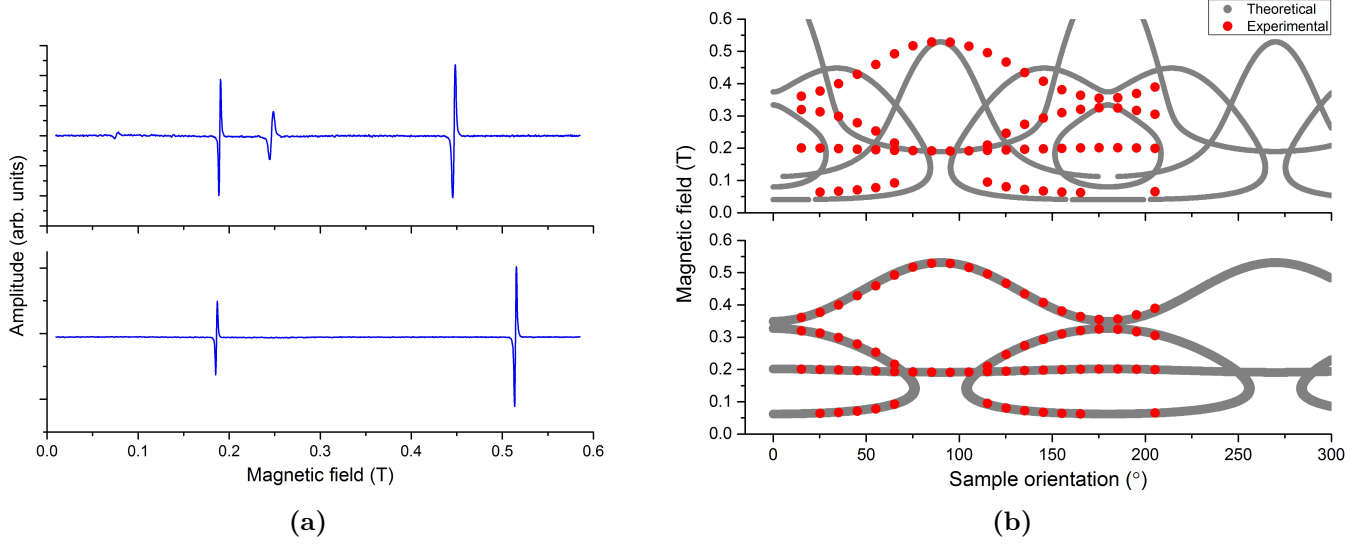
## 3.2 Experiment and Results

An irregularly shaped piece of ruby was used, with approximate dimensions 5mm×4mm×2mm. The sample was rotated in 10° increments, with ESR spectra recorded at each step. In total a 200° range of orientation was covered. For each spectrum, the magnet current was swept over its full range ($0 - 20\,\mathrm{A}$), corresponding to a field ranging from $0\,\mathrm{T}$ to $\sim 0.58\,\mathrm{T}$.

Generally four transitions are observed, and their positions and intensities change as a function of orientation $\theta$. For some angles certain transitions disappear completely. Examples of spectra I obtained are presented in Figure 4a. The settings used to obtain these were:

$$T = 500\,\mathrm{s}, \tau = 300\,\mathrm{ms}, I = 0 - 20\,\mathrm{A}.$$

In Figure 4b, spectra have been collated into a resonance field plot. I attempted to fit this data to a theoretical plot I had computed, using initial values $g_\parallel = 1.9840$, $g_\perp = 1.9867$ and $D = 5.747\mathrm{GHz}$ as obtained by Schulz-Dubois[1]. At first however, experimental and theoretical data did not agree.

I soon realised that I had not properly considered the crystal orientation. The theoretical model leading to

**Figure 4:** (a) ESR spectra for orientations $\theta = 65°$ (top) and $\theta = 95°$. (b) The resonance field is plotted as a function of $\theta$ and compared to theory. Top: the theoretical plot before inclination of the crystal axis to the horizontal was considered. Bottom: agreement between theory and experiment is found when an inclination $\chi \approx 66°$ is accounted for.

the computed resonance field assumes that the c-axis and the **B**-vector lie in the horizontal plane. Of course, there was no guarantee that the c-axis was oriented in this way. I therefore posited that the c-axis was in fact inclined at an angle $\chi$ to the horizontal, and built this into my computer model. This is easily done by considering the fact that originally $\theta$ is the angle between the c-axis and **B**. It is then simple geometry (Figure 5) to show that the transformation $\theta \rightarrow \cos^{-1}(\cos\theta\cos\chi)$ accounts for the inclination, where $\theta$ is now the angle between **B** and the projection of the c-axis onto the horizontal plane, and $\chi$ the angle between the c-axis and the horizontal plane. By varying $\chi$ in the model, good agreement between experiment and theory was found for $\chi \approx 66°$.

To finish, I wrote a 'best-fit' algorithm to find the parameter values that produce the minimum average discrepancy between experimental and theoretical data points. A brute force method was used, with the discrepancy calculated for a range of combinations of the

four parameters $g_\parallel$, $g_\perp$, $D$ and $\chi$. The final values obtained are displayed in Table 1. The uncertainties reflect the method of the algorithm. For example, the discrepancy is calculated for values of $g_\parallel$ which differ by 0.0010. The algorithm finds that the discrepancy is smaller for $g_\parallel = 1.9830$ than for 1.9820 and 1.9840. This suggests that the true value lies closer to 1.9830 than the two adjacent values, and hence a final value of $1.9830 \pm 0.0005$ is given. All values agree within uncertainty with previous studies, with the exception of $g_\perp$ when compared to Schulz-Dubois. The difference is $\mathcal{O}(10^{-4})$, and is possibly caused by the fact that the values have been obtained by different methods.

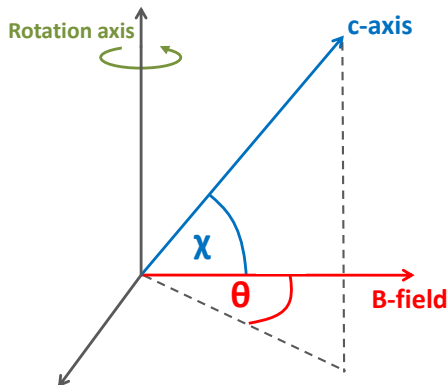|  | This study | Collins | Schulz-Dubois |
|---|---|---|---|
| $\nu$/GHz | $9.25 \pm 0.01$ | 9.33 | 9.30 |
| $g_\parallel$ | $1.9830 \pm 0.0005$ | $1.98 \pm 0.01^*$ | $1.9840 \pm 0.0006$ |
| $g_\perp$ | $1.9850 \pm 0.0005$ | $1.98 \pm 0.01^*$ | $1.9867 \pm 0.0006$ |
| $D$/GHz | $5.740 \pm 0.005$ | $5.71 \pm 0.05$ | $5.747 \pm 0.003$ |
| $\chi$/° | $66.40 \pm 0.05$ | | |

*Collins et al neglect g-factor anisotropy.*

**Table 1:** Values obtained for the parameters of the ruby spin Hamiltonian by using a best-fit algorithm to match theoretical and experimental data. Results of previous studies are given for comparison.
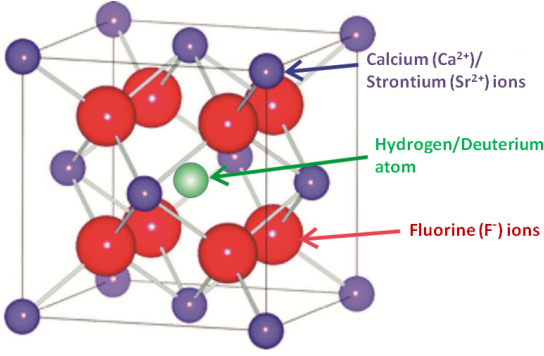
## 4   Atomic Hydrogen

### 4.1   Theory and Background

Studies of $CaF_2$:H, $SrF_2$:H and $CaF_2$:D are described in this section. I first discuss the spin Hamiltonian of these samples and its consequences for the ESR spectra, largely inspired by H&S and Nicholas[26].



**Figure 5:** An angle $\chi$ is introduced to account for the inclination of the crystal axis from the horizontal.

**Figure 6:** The unit cell of $CaF_2$ and $SrF_2$, with hydrogen/deuterium inserted into the interstitial space at the body-centre. Image taken from *MPhys Projects Trinity Term 2014* booklet[26].

$CaF_2$ and $SrF_2$ have a face-centred cubic lattice structure, with a basis

$$\text{Ca/Sr at } [000]$$
$$\text{F at } [\tfrac{1}{4}\tfrac{1}{4}\tfrac{1}{4}].$$

The samples used were originally prepared by annealing $CaF_2$ and $SrF_2$ in a hydrogen atmosphere and irradiating with X-rays to create the atomic hydrogen, which sits in the body-centre position of the unit cell. The resulting structure is shown in Figure 6.

We expect to observe transitions between the energy levels of the central hydrogen atom. A Hamiltonian describing these is[3][27]

$$H = g\mu_B \mathbf{B} \cdot \mathbf{S} + A\mathbf{I} \cdot \mathbf{S} - g_p \mu_N \mathbf{B} \cdot \mathbf{I} \\ + \sum_{i=1}^{8} (A_i^F \mathbf{S} \cdot \mathbf{I}_i^F - g_F \mu_N \mathbf{B} \cdot \mathbf{I}_i^F). \quad (8)$$

From left to right the terms are: the Zeeman interaction of the electron with the **B**-field; the electron-proton hyperfine interaction; the Zeeman interaction of the proton; the electron-fluorine hyperfine interaction; the Zeeman interaction of the fluorine. The sum is over the hydrogen atom's eight nearest-neighbour fluorine ions only. The relevant quantum numbers are the electron spin $S = 1/2$, the proton spin $I = 1/2$, and the fluorine nuclear spin $I^F = 1/2$.

In fact, since the nuclear magneton $\mu_N$ is so comparatively small, we have $A_i^F \mathbf{S} \cdot \mathbf{I}_i^F \gg g_F \mu_N \mathbf{B} \cdot \mathbf{I}_i^F$ for typical field strengths used in this experiment, and the latter term can be neglected. The Hamiltonian then possesses complete axial symmetry about the [111] directions of the crystal lattice. The electron-fluorine hyperfine coupling tensor $A_i^F$ can therefore be written in terms of just two components, $A_i^{\parallel}$ and $A_i^{\perp}$, parallel and perpendicular to the [111] axis.

Transitions obey the selection rules $\Delta M_S = \pm 1$ and $\Delta M_I = 0$, so we expect the ESR spectra to consist of two identical sets of lines corresponding to **S** and **I** being either parallel or antiparallel, with their separation dependent on the hyperfine coupling constant $A$.

The two sets of lines possess a substructure (henceforth *superhyperfine* structure) due to the electron-fluorine hyperfine interaction. Because of the crystal symmetry, this is easily analysed when the magnetic field is oriented along certain symmetry directions. The fluorine nuclear spins $\mathbf{I}_i^F$ point along the [111] directions due to the axial symmetry, and the spin of the electron **S** follows **B** due to its Zeeman interaction. Consider the case $\mathbf{B}\|[100]$. The angle between **S** and $\mathbf{I}_i^F$ is $\sim 55°$, so each $\mathbf{I}^F$ has a component either parallel or antiparallel to **S**. The 9 possible combinations (8 parallel, 0 antiparallel; 7 parallel, 1 antiparallel etc.) give 9 different values for the total electron-fluorine hyperfine energy, so we expect 9 distinct lines in the ESR spectrum. The relative intensities of these superhyperfine lines will depend mostly on the degeneracy of the configurations, e.g. there are $\binom{8}{5} = 56$ ways to have 5 fluorine spins parallel and 3 antiparallel to **S**. Thus an intensity ratio 1:8:28:56:70:56:28:8:1 is predicted.

Now consider $\mathbf{B}\|[111]$. One pair of fluorines have $\mathbf{I}^F$ at 0° to **S**, whilst for the other three pairs the angle is $\sim 71°$. The combinatorics predict 21 different superhyperfine lines. However, the lattice dimensions in the $CaF_2$:H crystal are such that the ratio $A_i^F I_i^F|_{0°} : A_i^F I_i^F|_{71°}$ is almost exactly 2, which reduces the number of lines to 11. An intensity ratio 1:6:17:32:46:52:46:32:17:6:1 is predicted by calculating the degeneracy.

The energy levels of the $CaF_2$:D sample should also be given by a Hamiltonian of the form (8). There is one key difference compared to the $CaF_2$:H sample however: the presence of a neutron makes the deuterium nucleus a spin-1 state, i.e. it has spin quantum numbers $I = 1$, $M_I = 0, \pm 1$. Thus we expect the electron-proton hyperfine splitting to lead to *three* evenly spaced sets of identical transition lines corresponding to the three values of $M_I$.
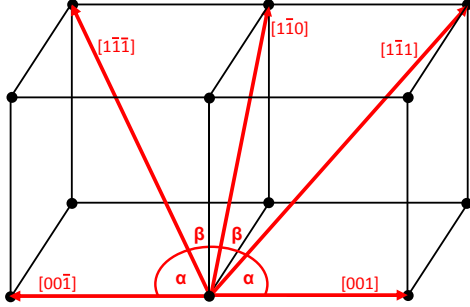
## 4.2 Experiment and Results

The crystals are cleaved in the (110) plane, and positioned so that this plane lies parallel to the horizontal. The orientations discussed above are then easily accessible by rotation of the sample holder (Figure 7).

The procedure for finding the desired crystal orientations is rudimentary. The sample holder is rotated by small amounts, with spectra recorded at each step. When the spectra begin to take the form of one of those described in the previous section, smaller rotations are made so as to gradually hone in on a precise crystal orientation. Once one such orientation is found and identified (by inspection and by measuring the intensity ratios of the lines), the others can be located

| Sample | | $\nu$/GHz | $g/g_e$ | $A$/MHz | $A_\parallel$/MHz | $A_\perp$/MHz |
|---|---|---|---|---|---|---|
| CaF$_2$:H | This study | $9.25 \pm 0.01$ | $1.00025 \pm 0.00004$ | $1461.1 \pm 0.5$ | $174.009 \pm 0.400$ | $68.957 \pm 0.400$ |
| | H&S[3] | 9 | $1.00023 \pm 0.00003$ | * | $173.826 \pm 0.300$ | $69.025 \pm 0.300$ |
| | Hodby[27] | X-band | * | * | 174.77 | 68.91 |
| SrF$_2$:H | This study | 9.25 | $1.00022 \pm 0.00004$ | $1441.04 \pm 0.5$ | $128.232 \pm 0.400$ | $44.022 \pm 0.400$ |
| | Hodby | X-band | * | 1440.94 | 127.45 | 43.55 |
| | Welber[4] | X-band | $1.00017 \pm 0.00003$ | $1442.0 \pm 0.2$ | $133.0 \pm 0.3$ | $46.0 \pm 0.3$ |

*No value given*

**Table 2:** Experimental results for the CaF$_2$:H and SrF$_2$:H samples, taken under standard conditions. For direct comparison, values obtained in my investigation are given alongside those of previous studies.
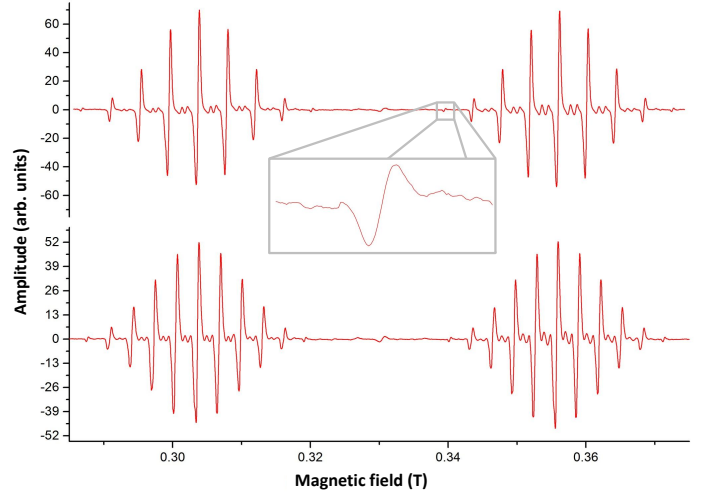


**Figure 7:** The symmetry directions accessible for the CaF$_2$ and SrF$_2$ crystals if oriented such that the (110) plane lies parallel to the horizontal. The angles between the symmetry directions are $\alpha \approx 55°$, $\beta \approx 35°$.



**Figure 8:** ESR spectra for CaF$_2$:H with **B**‖[100] (top) and **B**‖[111] (bottom). In each case, two sets of lines are seen due to the electron-proton hyperfine coupling. In each set there are 11/9 main transition lines in the [111]/[100] direction. This agrees with the prediction made by considering only nearest-neighbour electron-fluorine interactions. Doublets of much weaker transition lines corresponding to the "forbidden" selection rule $\Delta M_F = \pm 1$ are seen between the main lines. These have greater magnitude in the upper field set of lines.

more easily using the geometry of Figure 7. It is found that the crystal orientation had to be precise to less than 1° to produce the predicted intensity ratios.

Figure 8 shows spectra obtained for the CaF$_2$:H sample. Qualitatively they look as described in the previous section, with 9 transitions for **B**‖[100] and 11 for **B**‖[111]. In addition there are two smaller transition lines in between each main line. These occur because some of the approximations made break the crystal symmetry, allowing for transitions which obey the "forbidden" selection rule $\Delta M_F = \pm 1$. The intensities of the forbidden lines are greater in the high field set, as predicted by H&S and observed by Welber[4]. The settings used to obtain these spectra were

$$T = 700\,\text{s}, \tau = 300\,\text{ms}, I = 7.4 - 10.7\,\text{A}.$$

The g-factor and electron-proton hyperfine coupling $A$ are found by first determining the position of the central superhyperfine line in both the upper and lower field lineset. This line corresponds to the fourth term in the Hamiltonian (8) being zero. The *Breit-Rabi* formula[28] is employed to yield the eigenvalues of the first three terms of the Hamiltonian. Finally, by imposing the selection rules for the two lines, resonance conditions for the high and low field lines are found. These are solved simultaneously to obtain values of $g$ and $A$. This procedure has been used to determine values from [100] and [111] spectra and the final values, displayed

in Table 2, are an average of the two. The discrepancy between the two is due mainly to imprecision of the crystal orientations. A more detailed description of this calculation is provided in Appendix F.
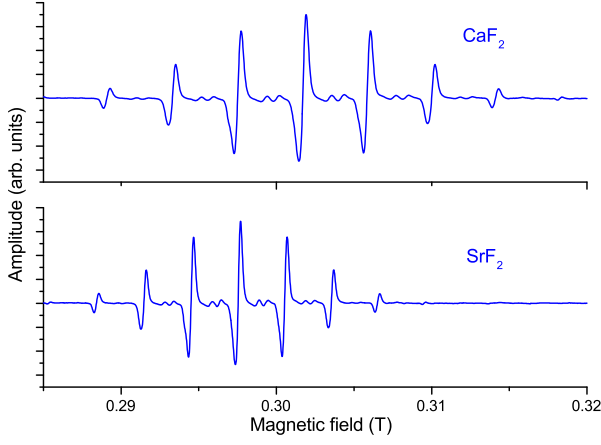
The components $A_\parallel$ and $A\perp$ of the electron-fluorine hyperfine tensor are determined using an expression given by H&S:

$$\delta B^2 = \frac{1}{(g\mu_B)^2}[A_\perp^2 + (A_\parallel^2 - A_\perp^2)\cos^2\theta] \qquad (9)$$

where $\theta$ is the angle between **B** and the [111] axis, and $\delta B$ is the magnetic field splitting between adjacent superhyperfine transitions. Using the g-factor calculated from the Breit-Rabi formula, the hyperfine components are found from the gradient and intercept of a plot of $\delta B^2$ versus $\cos^2\theta$. The results are also given in Table 2.

Figure 9 shows a comparison of the [100] ESR spec-

**Figure 9:** ESR spectra of $CaF_2$:H and $SrF_2$:H in the [100] direction. The superhyperfine line spacing is $\sim 1.6$ times smaller in $SrF_2$ than in $CaF_2$.
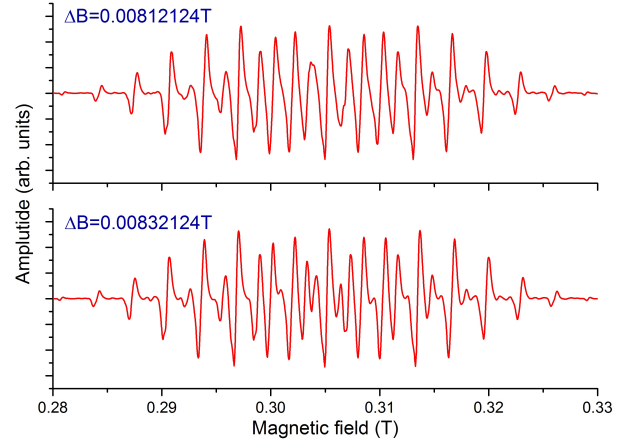
**Figure 10:** Model ESR spectra for $CaF_2$:D along the [111] direction constructed from three $CaF_2$:H spectra. TOP: electron-deuteron hyperfine splitting taken from Hall and Schumacher. BOTTOM: splitting increased by 0.0002T, producing a qualitatively different looking pattern.

tra for $CaF_2$:H and $SrF_2$:H. It is seen that the spacing between superhyperfine lines is smaller in $SrF_2$: $\delta_{Sr} \approx 0.63\delta_{Ca}$. This occurs because the two crystals have different lattice constants: $0.5463\,$nm and $0.5799\,$nm for $CaF_2$ and $SrF_2$ respectively[29]. This means that in $SrF_2$:H the electron is, on average, further from the F ions than in $CaF_2$:H, so their interaction is weaker. Parameters are calculated as for the $CaF_2$:H specimen, and the results presented in Table 2.

Of particular interest is the value $A$, which is $A(\text{free}) = 1420.406\,$MHz for the free hydrogen atom. This is the infamous 21cm spectral line whose detection is used extensively in cosmology and radio astronomy[30,31]. From my data, we calculate ratios of $A(CaF_2)/A(\text{free}) = 1.0286 \pm 0.0003$ and $A(SrF_2)/A(\text{free}) = 1.0145 \pm 0.0003$. The hydrogen atom is behaving as "nearly free", more so in $SrF_2$ due to the larger lattice spacing.

### 4.3 $CaF_2$:D

H&S found the electron-deuteron hyperfine coupling constant to be $\sim 6.5$ times smaller than the electron-proton coupling. This is sufficiently small that the three linesets should overlap, and the ESR spectra should reflect a superposition of the lines. The appearance of the spectra will depend on the precise value of the hyperfine coupling, and of course the precise orientation of the crystal. As such, it is difficult to envisage exactly what the spectra will look like, even along the symmetry directions.
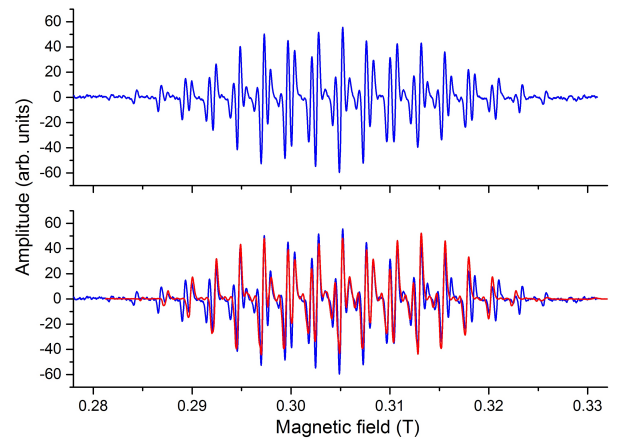
We are aided by the fact that we have good $CaF_2$:H data. I used this to construct $CaF_2$:D spectra by superposing three $CaF_2$:H spectra, with two offset from the other by equal and opposite amounts. To obtain accurate models, I first manipulated the $CaF_2$:H data to account for the slightly smaller values of $A_{\parallel}$ and $A_{\perp}$ in $CaF_2$:D, as found by H&S. I then superposed

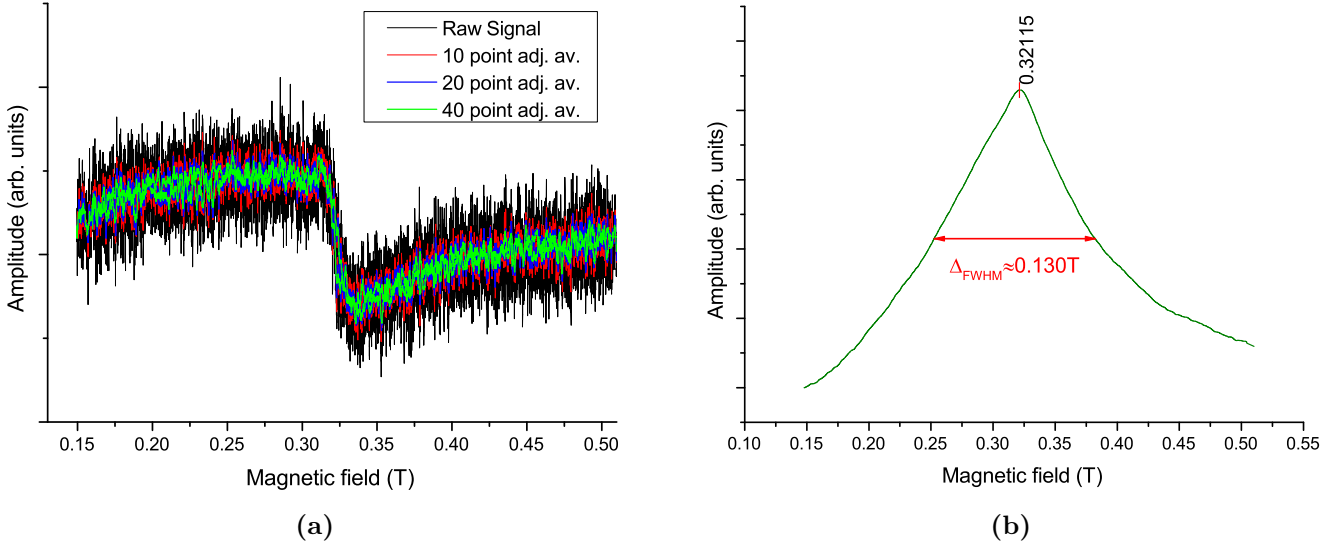three spectra using the value $A = 224.927$MHz found by H&S as a starting point, and made the approximation that the field offset matches the hyperfine coupling constant (converting to field units by multiplying by $^h/_{g\mu_B}$, using the free electron g-factor). Spectra were constructed for many different splittings, and two examples are shown in Figure 10. Modelling the spectra in this way does not appear to have been done before and is a neat way of visualising the $CaF_2$:D ESR spectra.

An ESR spectrum I obtained experimentally is shown in Figure 11. Whilst it bears some resemblance to the models in Figure 10, there are marked differences. I produced a better model by measuring the ap-



**Figure 11:** TOP: Experimental ESR spectra of $CaF_2$:D. The number of lines present suggests this orientation is close to the [111] direction. BOTTOM: Model spectrum (red) superimposed on experimental data (blue). The model was created by superposition of $CaF_2$:H spectra, and rescaling the splittings to match the experimental spectrum. There is very good agreement in the central region, but clear discrepancy for the outer lines. This suggests that the experimental data was taken with the crystal axis not quite aligned precisely parallel to [111].

**Figure 13:** ESR spectra of SWNT-P3HT composite, showing a resonance at $\sim 0.32$T. (a) Raw data, with several adjacent-average smoothing algorithms overlaid. (b) Integrating the raw signal removes most of the noise.

parent hyperfine and superhyperfine splittings in the experimentally obtained spectrum, and rescaling the CaF$_2$:H spectra to fit those values. This produces good agreement in the central region of the spectrum, but discrepancy towards the edges. I put this down, at least in part, to the crystal not being aligned precisely along a [111] direction. I found pinning down the symmetry directions incredibly difficult, as the qualitative structure of the spectra change significantly for the smallest of rotations. The settings used to obtain this spectrum were

$$T = 700s, \tau = 300\text{ms}, I = 7.7 - 10.5\text{A}.$$

A paper by Blum[32] shows a spectrum obtained precisely along the [111] direction (Figure 12). This spectrum was reproduced almost exactly by changing the splitting in my model to $0.00832 \pm 0.00009$T $\equiv 233.2 \pm 2.5$MHz, as in the bottom diagram of Figure 10. Blum's spectrum is taken at 4106 bar, increasing the value of $A$ by $\approx 160$kHz compared to H&S, i.e. $A \approx 225.1MHz$. The value I obtain is markedly different. The method I have used produces a result potentially more accurate than H&S, who comment that the accuracy of their results are limited by experimental factors such as transition lines being "washed

out" due to the interference. Caution should be taken in making a definitive conclusion however, given that I have not been able to obtain a spectrum at precise enough orientation to directly compare to my model. The value obtained is $\sim 1.06$ times larger than that of a free deuterium atom – a larger deviation from the free atom value than for hydrogen.
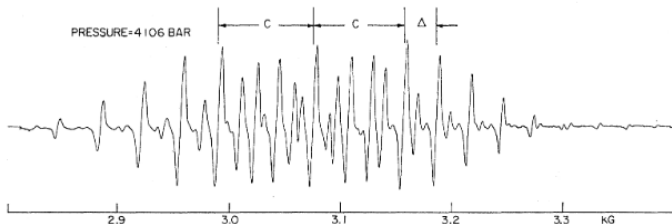
## 5    Carbon Nanotubes

In this final section, I discuss the results of an ESR investigation on a SWNT-P3HT nanohybrid composite. The sample was prepared in the Clarendon laboratory using drop-cast methods to coat a high concentration solution of nanotubes on to a quartz film. In principle, the polymer strands prohibit the nanotubes from interacting directly with one another, and the nanotubes should be randomly oriented on the film. A sample of pure P3HT was also prepared for use as a control.
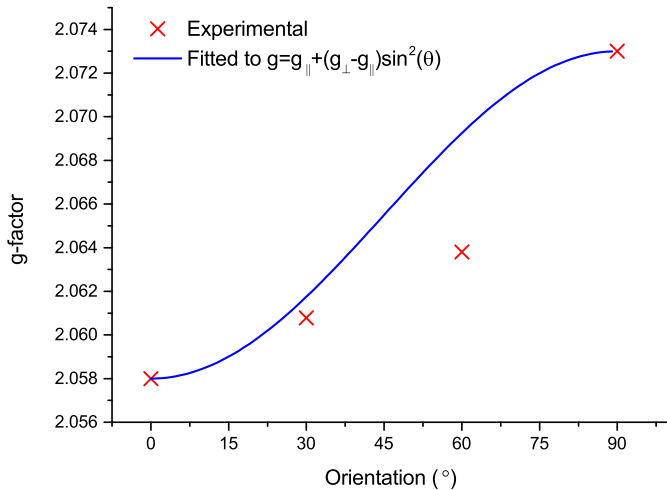
The sample was placed with **B** parallel to the plane of the film. Figure 13a shows the ESR spectrum I obtained. In an attempt to observe any subtle details in the spectrum, a very long time period was used in combination with a comparatively short time constant:

$$T = 2000s, \tau = 100\text{ms}, I = 0 - 20\text{A}.$$

This parameter choice leads to a very noisy signal, but nonetheless a prominent absorption peak is easily seen at $B \sim 0.32T$. Satisfyingly, the noise all but disappears when the raw signal is integrated (Figure 13b). The centre of the resonance is at $0.32115(40)$T, corresponding to a g factor of $g_{\parallel} = 2.058 \pm 0.003$. The full width at half maximum is $\Delta_{FWHM} = (0.1298 \pm 0.0004)$T. The asymmetric lineshape is similar to that obtained by Corzilius et al on a fullerene-SWNT composite. They state that this is characteristic of itin-



**Figure 12:** ESR spectrum of CaF$_2$:D in the [111] direction obtained at 4106 bar. Image taken from a paper by Blum[32].

**Figure 14:** A g-factor anisotropy is observed as the SWNT-P3HT coated film is rotated relative to **B**. An attempt is made to fit to an expression given by Konkin, but poor agreement is found.

erant conduction electrons[19]. It is therefore sensible to conclude that the presence of this line is due to delocalized electrons moving on the walls of the nanotubes. This idea is further supported by the findings of Chipara et al[20] on a polyethylene-SWNT composite. The lineshape is very different to Figure 1, and could perhaps be a superposition of many narrower transitions.

Spectra recorded for different orientations of the film relative to the field suggest a slight g-factor anisotropy (Figure 14). For **B** perpendicular to the film plane, $g_\perp = 2.073 \pm 0.003$ and $\Delta_{FWHM} = (0.1297 \pm 0.0004)$T. Konkin et al[33] have observed anisotropy in a *metallic* SWNT-P3HT sample which fits an expression derived by Chauvet et al[34] for aligned nanotubes. Such an expression should therefore not apply to our sample and, as seen in Figure 14, indeed it does not appear to. It is possible that the anisotropy is a cavity effect. The cavity only supports a single frequency mode in one direction, so the interaction may be slightly different with the film parallel and perpendicular to this mode. However, it is difficult to make any conclusions with great confidence seeing as the anisotropy is just a small fraction of the resonance linewidth.

I attempted to take measurements at 77K using a nitrogen cryostat, which in principle should produce signal intensities $\sim 4$ times stronger than room temperature. The cryostat consists of a thin quartz tube, which sits in the resonant cavity, connected to a large glass Dewar above. A vacuum pump is attached to the vacuum valve (shown in Figure 2a), which lowers the pressure so that the nitrogen does not boil away.

Unfortunately, numerous issues were encountered which meant that ultimately I was unable to collect good data at this temperature. At first, the nitrogen bubbled vigorously, and boiled away in $\sim 15$ minutes,

making long sweep times impossible. This problem was fixed after I located a leak in the apparatus, which was plugged with an epoxy material. Secondly, residue materials in the cryostat and resonant cavity were producing signals that dominated the ESR spectra. This was fixed by cleaning both extensively. Finally, and indeed fatally, the quartz tube was accidentally snapped away from the Dewar, rendering the cryostat unusable.

## 6 Conclusion

Calibration of the ESR kit has been well achieved, with parameters obtained for the ruby and hydrogen samples in good agreement with previous studies. For ruby, the theory described by Collins et al has been applied to build a computer program capable of plotting the resonance field for any chosen crystal orientation. Experimental data has been successfully fitted to this theoretical plot. A best-fit algorithm has determined that, as currently positioned, the c-axis lies at $66.40 \pm 0.05°$ to the horizontal. In future experiments, it would be beneficial to pin the crystal axis in the horizontal plane, as this would allow measurements of $g$ and $D$ to be taken directly. This would offer a more valid comparison with the studies of Schulz-Dubois and Collins.

Well-resolved spectra have been obtained for the [100] and [111] orientations of the $CaF_2$ and $SrF_2$ crystals. The number of transition lines in these spectra, and their relative intensities, agree with the predictions of H&S, validating their mathematical model of the system. The g-factor and electron-proton hyperfine coupling are closer to that of a free hydrogen atom in the $SrF_2$ crystal. This is because $SrF_2$ has a larger lattice constant, and hence the effect of the F ions on the hydrogen atom is weaker.

A method has been devised for modelling the $CaF_2$:D spectra using experimentally obtained $CaF_2$:H data. This method suggests a possible correction to the electron-deuteron hyperfine coupling found by H&S – the value proposed here is $233.2 \pm 2.5$MHz at 4106 bar. The quality of experimental data for this sample has been limited by the precision with which the sample could be rotated by hand. Development of an automated system for rotation could produce more precisely oriented spectra. By then fitting these to model spectra, a more accurate value of the hyperfine coupling may be obtained.

A single broad, prominent transition has been observed in the SWNT:P3HT composite at $B \approx 0.32T$. The asymmetric lineshape is indicative of itinerant electrons. I have therefore posited that the presence of this line is due to itinerant electrons moving on the nanotube walls, as supported by the studies of Corzilius et al and Konkin et al. An anisotropy has been ob-

served in the g-factor of the transition, with extremal values $g_\parallel = 2.058 \pm 0.003$ and $g_\perp = 2.073 \pm 0.003$ obtained. However, since the anisotropy is a small fraction of the resonance linewidth, it is hard to make definitive conclusions. Intuitively, we would not expect anisotropy since the nanotubes are randomly oriented on a quartz film, and the observed anisotropy may be a cavity effect.

I have attempted to take measurements at 77K, but the breakage of the nitrogen cryostat has inhibited my investigations. Low temperature measurements could potentially shed more light on the apparent g-factor anisotropy. It is also possible that additional resonances may be resolved at low temperature. For example, for a polyethylene-SWNT composite Chipara has observed a weak, narrow resonance near to the peak of the broad resonance. Such a line is not observed in my room temperature spectra. If it were also not seen at low temperature, a clear difference in the ESR spectra of the two composites would be identified. The cryostat should be fixed by mid-May, and I hope to carry out low temperature measurements then. The temperature dependence of the ESR spectrum could be further investigated by taking measurements over a wide range of temperature.

# References

[1] EO Schulz-Dubois, Bell System Technical Journal **38**, 271 (1959)

[2] LA Collins, MA Morrison and PL Donoho, American Journal of Physics **42**, 560 (1974)

[3] JL Hall and RT Schumacher, Physical Review **127**, 1892 (1962)

[4] B Welber, Physical Review **136**, A1408 (1964)

[5] S Iijima, T Ichihashi, T. Nature **363**, 603 (1993)

[6] DS Bethune, CH Klang, MS de Vries, G Gorman, R Savoy, J Vazquez and R Beyers, Nature **363**, 605 (1993)

[7] M Monthioux and VL Kuznetsov, Carbon **44**, 1621 (2006)

[8] SB Sinnott and R Andrews, Critical Reviews in Solid State and Materials Sciences **26**, 145 (2001)

[9] TH Cho, WS Su, TC Leung, Wei Ren and CT Chan, Computer Physics Communications **184**, 1077 (2013)

[10] T Schuettfort, HJ Snaith, A Nish and RJ Nicholas, Nanotechnology **21** 025201 (2010)

[11] A Nish, JY Huang, J Doig and RJ Nicholas, Nature Nanotechnology **2**, 640 (2007)

[12] JA Alexander-Webber, C Faugeras, P Kossacki, M Potemski, X Wang, HD Kim, SD Stranks, RA Taylor and RJ Nicholas, Nano Lett. **14**, 5194 (2014)

[13] W Gomulya, J Gao and MA Loi, Eur. Phys. J. B **86**, 404 (2013)

[14] J You, L Dou, K Yoshimura, T Kato, K Ohya, T Moriarty, K Emery, C-C Chen, J Gao, G Li and Y Yang, Nature Communications **4**, 1446 (2013)

[15] MA Green, K Emery, Y Hishikawa and W Warta, Prog. Photovolt. **16**, 61 (2008)

[16] T Dürkop, SA Getty, E Cobas and MS Fuhrer, Nano Lett. **4**, 35 (2004)

[17] H Zhu, J Wei, K Wang and D Wu, Solar Energy Materials and Solar Cells **93**, 1461 (2009)

[18] M Lanzi, L Paganin and D Caretti, Polymer **49**, 4942 (2008)

[19] B Corzilius, A Gembus, N Weiden, K-P Dinse and K Hata, Phys. Stat. Sol. (b) **243**, 3273 (2006)

[20] M Chipara, K Lozano, R Wilkins, EV Barrera, MX Pulikkathara, L Penia-Para and M Chipara, J. Mater. Sci. **43**, 1228 (2008)

[21] RJ Nicholas, *SS12 Paramagnetic Resonance* lab script, `http://goo.gl/15DNYq` (may require Oxford single sign-on)

[22] *Crystallography365* online blog, `http://goo.gl/hBLizC`

[23] MHL Pryce, Proc. Phys. Soc. A **63**, 25 (1950)

[24] C Kikuchi, J Lambe, G Makhov and RW Terhune, Journal of Applied Physics **30**, 1061 (1959)

[25] Aripin, S Mitsudo, T Shirai, K Matsuda, T Kanemaki, T Idehara and T Tatsukawa, International Journal of Infrared and Millimetre Waves **20**, 1875 (1999)

[26] RJ Nicholas, *MPhys Projects Trinity Term 2014* booklet, `http://goo.gl/jaFlXp` (may require Oxford single sign-on)

[27] JW Hodby, Journal of Physics C: Solid State Physics **2**, 404 (1969)

[28] G Breit and II Rabi, Physical Review **38**, 2082 (1931)

[29] WK Liu and MB Santos, *Thin Films: Heteroepitaxial Systems*, World Scientific Publishing Co. Pte. Ltd. (1999), p.214

[30] JR Pritchard and A Loeb, Rep. Prog. Phys. **75**, 086901 (2012)

[31] S Furlanetto, S Peng Oh and F Briggs, Phys. Rept. **433**, 181 (2006)

[32] H Blum, Physical Review **161**, 213 (1967)

[33] A Konkin, C Bounioux, U Ritter, P Scharff, EA Katz, A Aganov, G Gobsch, H Hoppe, G Ecke and H-K Roth, Synth. Met. **161**, 2241 (2011)

[34] O Chauvet, L Forro, W Bacsa, D Ugarte, B Doudin and WA de Heer, Phys. Rev. B **52**, R6963 (1995)

[35] JA McMillan, *Electron Paramagnetism*, Reinhold Book Corporation (1968), pp.183-184

[36] JE Wertz and JR Bolton, *Electron Spin Resonance: Elementary Theory and Practical Applications*, Chapman and Hall (1986), p.465

[37] S Blundell, *Magnetism in Condensed Matter*, OUP (2001), pp. 45-48

[38] HE Radford, VW Hughes and V. Beltran-Lopez, Physical Review **123**, 153 (1961)

[39] B Odom, D Hanneke, B D'Urso and G Gabrielse, Physical Review Letters **97**, 030801 (2006)

# Appendix A: Magnetic field calibration

A Hall probe enables the magnetic field strength to be directly measured. The probe is fixed in place such that magnetic field lines cut through the sensor at right angles. A DC current is passed through the sensor, leading to the development of a *Hall voltage* $V_H$ mutually perpendicular to the current and field. The PC reads the Hall voltage from the probe. A linear relationship between voltage and field is predicted: $B = aV_H + b$. Values for $a$ and $b$ must be found to calibrate the field strength.
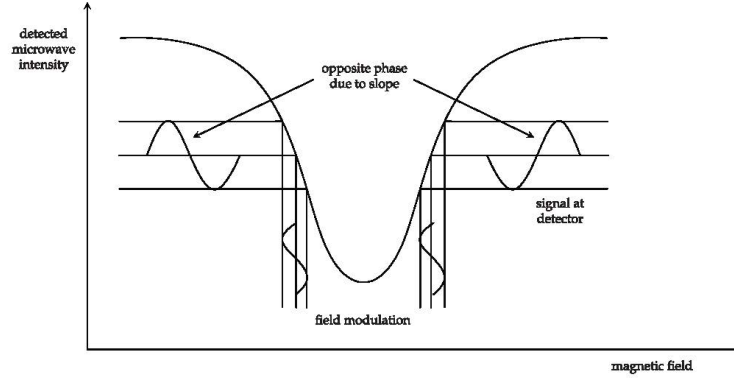
This is done by taking readings of the Hall voltage for a range of magnet supply currents. At each current, the magnetic field is determined using the *nuclear magnetic resonance* (NMR) of protons in water. An NMR probe containing this sample is positioned in the magnetic field and the NMR signal displayed on an oscilloscope. By measuring the frequency at which the NMR signal occurs, a magnetic field value can be deduced using the fact that the NMR of protons occurs at $42.5759\text{MHzT}^{-1}$.

$V_H$ is plotted against $B$, and a linear fitting imposed. Values of $a = (0.1083 \pm 0.0002)\text{T/V}$ and $b = -(0.0007 \pm 0.0004)\text{T}$ are found. The uncertainties reflect the fact that the relationship is not precisely linear. These values are inputted into the data acquisition software so that the Hall voltage can be converted to magnetic field instantaneously. Previously, this calibration using the NMR probe would have to be done for each new spectrum but, with the introduction of the Hall probe, this is no longer the case. The procedure is carried out for both upward and downward sweeps of the magnet current, as the relationship between current and field may differ in the two directions due to hysteresis. The slight nonlinearity between $V_H$ and $B$ is the means an error is incurred by using the Hall probe to measure the field, compared to using the NMR probe directly. The error is small however, and the ease with which data can be taken with the Hall probe more than compensates the slight loss of accuracy.

This calibration is not completely accurate due to difficulty in determining the frequency of the NMR signal. To overcome this issue, the magnetic field is recalibrated for all spectra by using DPPH as a "g-marker". Historically, DPPH is often used to calibrate the magnetic field because it produces a single resonance which is incredibly strong and narrow. The narrowness arises from an exchange interaction, whereby the spin orientation of the unpaired electrons is exchanged between orbitals[35]. The g-factor of DPPH is accurately known to be $2.0037 \pm 0.0002$[36]. From Equation (1) it is easily deduced that the absorption peak should appear at a field of 0.32983T. We recalibrate the field by pinning the value of $b$, and multiplying the field values such that the centre of the DPPH absorption peak lies at 0.32983T.

# Appendix B: Phase-sensitive detection

As stated in Section 2, phase-sensitive detection (PSD) is employed to improve the signal-to-noise ratio of the ESR signal. Here I discuss how this is achieved and explain why it results in the output signal looking like the derivative of the ESR absorption spectrum. This section borrows heavily from Appendix B of the SS12 lab script[21].
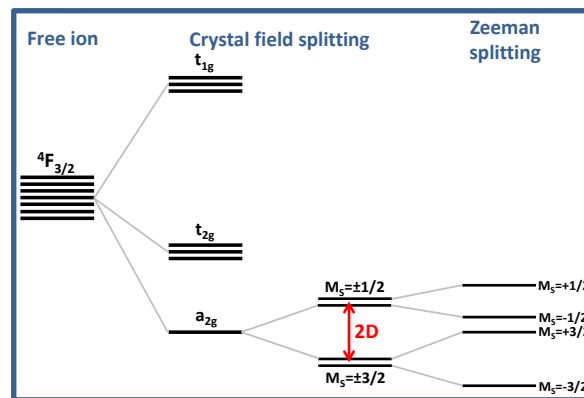


**Figure 15:** Visualisation of phase-sensitive detection, showing how the output signal looks like the derivative of the absorption with respect to field.

A single loop of wire, driven by a *115kHz oscillator*, modulates the magnetic field in the vicinity of the sample. The signal from the detector diode is fed to the input of a *lock in amplifier*, via a pre-amp tuned to 115kHz, as is the signal from the oscillator for use as a reference. The only components of the detector diode signal that pass through the lock-in amplifier unattenuated are those matching the 115kHz reference signal. By modulating up to 115kHz, we remove all low frequency noise from our signal. The output of the lock-in is fed to the PC.

A consequence of PSD is that the output signal looks like the derivative of the absorption spectrum with respect to field. This is because as the static field is swept, the small oscillatory field means that the absorption peak is swept through repeatedly, within its linewidth. This means each point of the lineshape is plotted, but takes on the shape of the oscillatory signal i.e. it looks like the derivative. This is visualised in Figure 15.

# Appendix C: The spin Hamiltonian of ruby



**Figure 16:** Development of the energy levels from that of a free $Cr^{3+}$ ion to those considered in an ESR experiment. The octahedral crystal environment splits the levels into 3 groups relative to that of the free ion (see Appendix A). The ground state is further split into two doublets by the crystal field, and the doublets then split by the application of a magnetic field.

Here the form of the Hamiltonian of Equation 5 is justified, following arguments from Collins et al.

By Hund's rules, a *free* $Cr^{3+}$ ion has a ground state configuration of $[Ar]3d^3$, with a term symbol $^4F_{3/2}$, i.e. the angular momentum quantum numbers are $S = {}^3/_2$, $L = 3$, $J = {}^3/_2$. The effect of the crystal field is to remove the $2L + 1 = 7$-fold spatial degeneracy. By applying basic crystal field theory (I do this explicitly in

Appendix D) this causes the ground state to split as in Figure 16, with the new ground state having no spatial degeneracy. It does however have a 4-fold spin degeneracy and, to a first approximation, these spin states can be treated as the eigenstates of a free spin (the aforementioned *effective* spin) with quantum number $S = 3/2$, i.e.

$$\hat{S}^2 |M_S\rangle = S(S+1) |M_S\rangle \tag{10}$$
$$\hat{S}_z |M_S\rangle = M_S |M_S\rangle \tag{11}$$

where the z-axis is parallel to the c-axis.

The crystal field acts so as to split these four levels into two doublets: one corresponding to $M_S = \pm 3/2$ and the other to $M_S = \pm 1/2$. This splitting is described by the second term in the spin Hamiltonian: it equals $+D$ for $M_S = \pm 1/2$ and $-D$ for $M_S = \pm 3/2$. Application of a magnetic field splits the two doublets into four distinct levels. It is transitions between these levels that are observed in an ESR experiment.

The Hamiltonian is diagonalized using a linear combination of spin eigenstates $|\phi_n\rangle = \sum_j A_{ij} |j\rangle$. A time-independent Schrödinger equation can then be written in matrix form

$$\begin{pmatrix} \langle \frac{3}{2} | H | \frac{3}{2} \rangle & \cdots & \langle \frac{3}{2} | H | \frac{-3}{2} \rangle \\ \vdots & \ddots & \vdots \\ \langle \frac{-3}{2} | H | \frac{3}{2} \rangle & \cdots & \langle \frac{-3}{2} | H | \frac{-3}{2} \rangle \end{pmatrix} \begin{pmatrix} A_{n1} \\ \vdots \\ A_{n4} \end{pmatrix} = E \begin{pmatrix} A_{n1} \\ \vdots \\ A_{n4} \end{pmatrix}$$

Using explicit forms of the spin-$\frac{3}{2}$ matrices it is readily shown that the energy eigenvalues are determined by solving
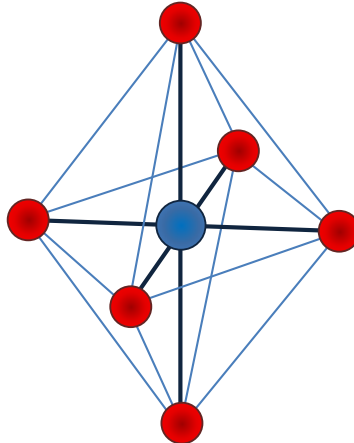
$$\begin{vmatrix} \frac{3C}{2} - D - E & \frac{\sqrt{3}}{2} S & 0 & 0 \\ \frac{\sqrt{3}}{2} S & \frac{C}{2} + D - E & S & 0 \\ 0 & S & -\frac{C}{2} + D - E & \frac{\sqrt{3}}{2} S \\ 0 & 0 & \frac{\sqrt{3}}{2} S & -\frac{3C}{2} - D - E \end{vmatrix} = 0$$

where $C = g_\parallel \mu_B B \cos\theta$ and $S = g_\perp \mu_B B \sin\theta$. This leads to (after some very tedious algebra) a quartic secular equation for the eigenvalues

$$\begin{aligned} E^4 &- \left( \frac{5}{2} \mu_B^2 B^2 \left( g_\perp^2 + \left( g_\parallel^2 - g_\perp^2 \right) \cos^2\theta \right) + 2D^2 \right) E^2 + 2D\mu_B^2 B^2 \left( \left( 2g_\parallel^2 + g_\perp^2 \right) \cos^2\theta - g_\perp^2 \right) E \\ &+ D^4 + \frac{9}{16} \mu_B^4 B^4 \left( g_\perp^2 + \left( g_\parallel^2 - g_\perp^2 \right) \cos^2\theta \right)^2 + \frac{1}{2} D^2 \mu_B^2 B^2 \left( g_\perp^2 - \left( g_\perp^2 + 5g_\parallel^2 \right) \cos^2\theta \right) = 0 \end{aligned} \tag{12}$$

This equation is solved numerically in my computer model.
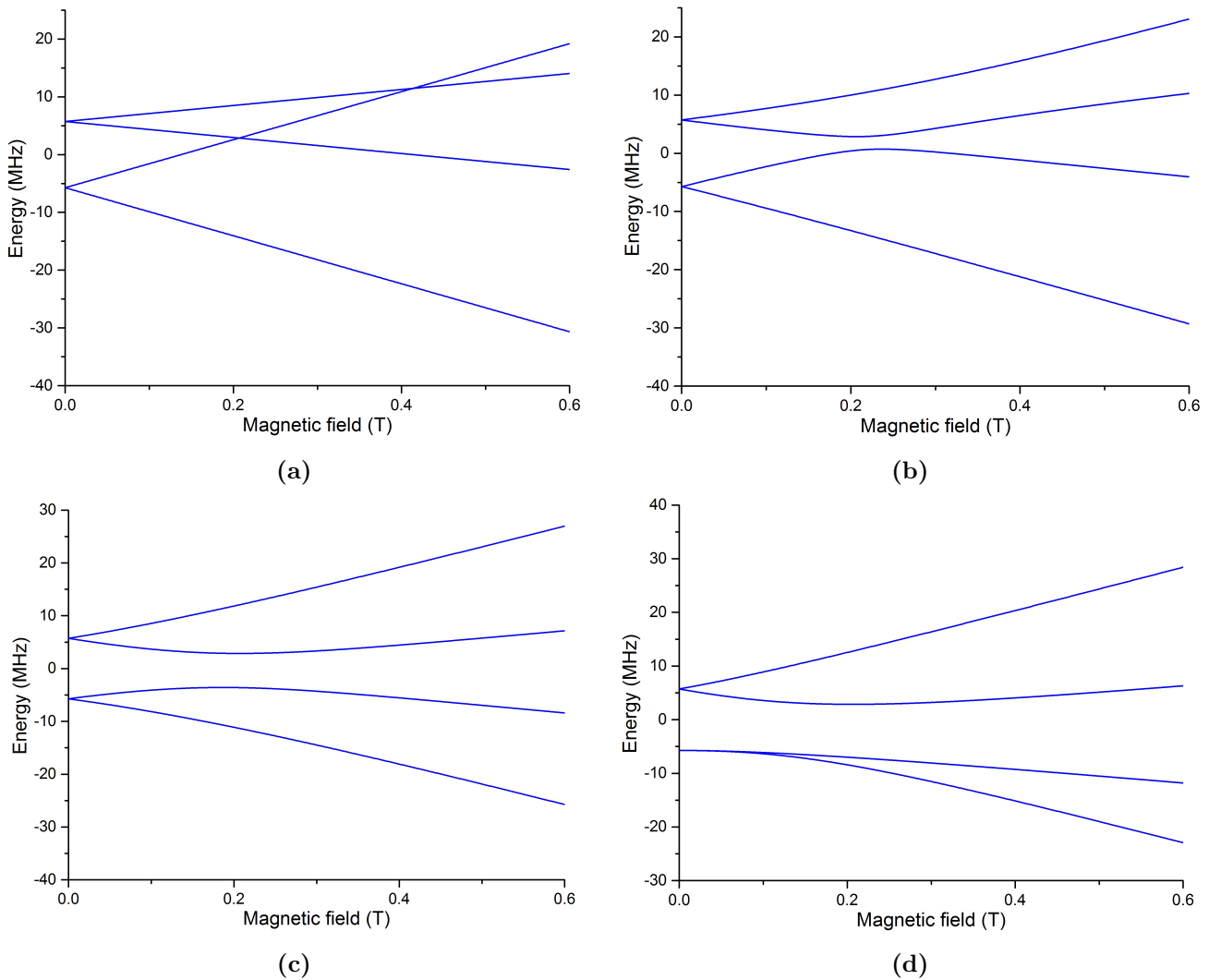
## Appendix D: f-orbitals in an octahedral crystal field



**Figure 17:** $Cr^{3+}$ ion enclosed in an octahedron of $O^{2-}$ ions, as found in ruby. The crystal field sourced by the $O^{2-}$ ions affects the energy levels of the central $Cr^{3+}$ ion significantly.

Here the crystal field splitting leading to the energy level structure in Figure 16 is justified, following arguments similar to those given by Blundell[37] for d orbitals in an octahedral field. The ground state of a free $Cr^{3+}$ ion has a ground state term symbol $^4F_{3/2}$, which is degenerate with respect to the quantum number $M_L$. When placed in an octahedral environment (see Figure 17), this degeneracy is partially broken. To see this, consider the nature of the 7 f-orbitals and how they interact with the p-orbitals of the $O^{2-}$ ions. Three of the f-orbitals (the so-called $t_{1g}$ orbitals) have a maximal overlap with the p-orbitals, and these states are thus raised in energy. One of the other f-orbitals (the $a_{2g}$ orbital) has a minimal overlap with the p-orbitals, and is thus lowered in energy. The three remaining f-orbitals (the $t_{2g}$) orbitals have an intermediate overlap with the p-orbitals. The crystal field therefore splits the seven previously degenerate levels into three distinct groups, as seen in Figure 16. The $a_{2g}$ orbital is the new ground state.

## Appendix E: Ruby energy level diagrams

Examples of the energy level diagrams for the ruby crystal, produced using a program that I had written, are given in Figure 18. The B-dependence of the levels is clearly $\theta$-dependent, implying transitions occur at different fields for different crystal orientations.



**Figure 18:** Energy level diagrams for (a) $\theta = 0°$, (b) $\theta = 30°$, (c) $\theta = 60°$, and (d) $\theta = 90°$. $\theta$ is the angle between the crystal axis and the B-field.

## Appendix F: Details of atomic hydrogen calculations

In Section 4.2, values for $g$, $A$, $A_{\parallel}$ and $A_{\perp}$ are derived using the Breit-Rabi formula[28] (here given in frequency units)

$$E(F, M_F) = -\frac{A}{4} - \frac{g_p \mu_N B M_F}{h} \pm \frac{A}{2}\left(1 + 2M_F x + x^2\right)^{1/2}, \tag{13}$$

where $x = \frac{(g\mu_B + g_p\mu_N)\mathrm{B}}{Ah}$, and $+$ goes with $F = 1$, $-$ with $F = 0$. $F$ and $M_F$ are the quantum numbers corresponding to the total angular momentum of the hydrogen atom $\mathbf{F} = \mathbf{S} + \mathbf{I}$. We consider the central superhyperfine transition of the upper and lower set of lines. The resonance condition is

$$
\begin{aligned}
\nu = E(1,1) - E(0,0) &= \frac{-g_p\mu_N\mathrm{B}_l}{h} + \frac{A}{2}\left[1 + \left(\frac{(g\mu_B + g_p\mu_N)\,\mathrm{B}_l}{hA}\right)^2\right]^{1/2} \\
&+ \frac{A}{2}\left[1 + 2\left(\frac{(g\mu_B + g_p\mu_N)\,\mathrm{B}_l}{hA}\right) + \left(\frac{(g\mu_B + g_p\mu_N)\,\mathrm{B}_l}{hA}\right)^2\right]^{1/2}
\end{aligned}
\tag{14}
$$

for the lower field line, and

$$
\begin{aligned}
\nu = E(1,0) - E(1,-1) &= \frac{-g_p\mu_N\mathrm{B}_u}{h} + \frac{A}{2}\left[1 + \left(\frac{(g\mu_B + g_p\mu_N)\,\mathrm{B}_u}{hA}\right)^2\right]^{1/2} \\
&- \frac{A}{2}\left[1 - 2\left(\frac{(g\mu_B + g_p\mu_N)\,\mathrm{B}_u}{hA}\right) + \left(\frac{(g\mu_B + g_p\mu_N)\,\mathrm{B}_u}{hA}\right)^2\right]^{1/2}
\end{aligned}
\tag{15}
$$

for the upper field line. From our resonance spectra, we measure the field positions of the upper and lower central superhyperfine lines $\mathrm{B}_u$ and $\mathrm{B}_l$. We then have two equations with two unknowns: $g$ and $A$. The two equations are simultaneously solved by computational methods to obtain values of these two parameters.

For example, from the [100] and [111] CaF$_2$:H spectra average values $\mathrm{B}_l = 0.30169\,\mathrm{T}$ and $\mathrm{B}_u = 0.35306\,\mathrm{T}$ are obtained. Plugging these into the above resonance conditions and solving, we find $A = 1461.1\,\mathrm{MHz}$ and $g = 2.00282 = 1.00025g_e$, where $g_e = 2.002319304$ is for a free electron (as found by Odom[39].)